Journal of Energy Storage 66 (2023) 107429

Contents lists available at ScienceDirect

Journal of Energy Storage

journal homepage: www.elsevier.com/locate/est

Research papers

Improving efficiency and discharge power of acid-base flow battery via a bi-objective optimisation

Andrea Culcasi [a], Luigi Gurreri [b,*], Alessandro Tamburini [a,*], Andrea Cipollina [a], I. David L. Bogle [c], Giorgio Micale [a]

[a] Dipartimento di Ingegneria, Università degli Studi di Palermo, Viale delle Scienze ed. 6, 90128 Palermo, Italy
[b] Dipartimento di Ingegneria Elettrica, Elettronica e Informatica, Università di Catania, Viale Andrea Doria 6, 95125 Catania, Italy
[c] Centre for Process Systems Engineering, Department of Chemical Engineering, University College London, Torrington Place, London WC1E 7JE, United Kingdom

ARTICLE INFO

Keywords:
Electro-chemical energy storage
Ion-exchange membrane
Flow battery
Bipolar membrane (reverse) electrodialysis
Modelling
Optimization

ABSTRACT

The implementation of effective storage systems is essential for a deeper market penetration of intermittent renewable sources. One promising, environmentally friendly energy storage technology is the Acid-Base Flow Battery (AB-FB). In the charge phase it stores electricity in the form of pH and salinity gradients via Bipolar Membrane Electrodialysis, while in the discharge phase it applies the reverse process for the opposite conversion. Despite the clear benefits over other osmotic batteries, the potential of the AB-FB has been poorly explored.

This study presents the first bi-objective optimisation of the AB-FB in terms of net round trip efficiency (RTE_{net}) and average net discharge power density per membrane area ($\overline{NPD_d}$). A comprehensive mathematical model previously developed by our research team was used to predict the battery performance. The ε-constraint approach was used to build curves of Pareto optimal solutions under various scenarios by letting several operating and design parameters to vary. Using current commercial membranes, optimal solutions yielded an RTE_{net} ranging from 32 % to 64 %, while the corresponding $\overline{NPD_d}$ ranged from 19.5 W m^{-2} to 4 W m^{-2}. These results highlight the great potential of the AB-FB, as well as the need of a proper design of experimental stacks. Simulating hypothetical membranes with improved, yet realistic characteristics shifted the range of RTE_{net} and $\overline{NPD_d}$ to 59.1–76.3 % and 23.2–4.4 W m^{-2}, respectively, showing that the technological advancement in membrane manufacturing is essential for the development of high-performance AB-FB systems. Although the AB-FB performs similarly to other batteries, it can be made of non-critical materials that are not subject to supply disruptions or economic dependency, making the AB-FB a sustainability-friendly option and a good candidate for the future energy storage systems scenario.

1. Introduction

The energy sector is one of the key players to address climate change by decarbonisation strategies [1]. The development and spread of technologies based on renewable energy sources are important in this sense. However, the mismatch between power generation and consumption is a major issue for renewable sources such as solar and wind [2]. Energy storage systems are essential to tackle this issue. Moreover, they act for grid stabilisation and rapid response to demand [3]. Effective systems should be MWh scalable, safe, environmentally friendly, robust, cost-effective, and independent of location. Different technologies have been proposed, and among them, flow batteries store energy in the form of electrolyte solutions [4–8]. Within this innovative group, Acid-Base flow batteries meet all the above-mentioned requirements, fit well with modern smart grids, and have high performance. The working principle of AB-FBs is related to the water dissociation reaction that occurs in the interlayer of the battery's bipolar membranes [9]. AB-FB combines two membrane processes, namely Bipolar Membrane Electrodialysis (BMED) during the charge phase and Bipolar Membrane Reverse Electrodialysis (BMRED) during the discharge phase [10] (Fig. 1).

In the AB-FB (Fig. 2), there are repeating units called triplets, each

Abbreviations: EES, Electro-chemical storage; AB-FB, Acid-base flow battery; BPM, Bipolar membrane; BMED, Bipolar membrane electrodialysis; BMRED, Bipolar membrane reverse electrodialysis; NPD, Net power density; RTE, Round-trip efficiency.

* Corresponding authors.
E-mail addresses: luigi.gurreri@unict.it (L. Gurreri), alessandro.tamburini@unipa.it (A. Tamburini).

https://doi.org/10.1016/j.est.2023.107429
Received 23 November 2022; Received in revised form 17 March 2023; Accepted 11 April 2023
Available online 26 April 2023
2352-152X/© 2023 The Authors. Published by Elsevier Ltd. This is an open access article under the CC BY-NC-ND license (http://creativecommons.org/licenses/by-nc-nd/4.0/).

comprising an anion-exchange membrane and a cation-exchange membrane (AEM and CEM), as well as a bipolar membrane (BPM), which is made up of a cation-exchange layer and an anion-exchange layer stacked on top of each other.

Ion-exchange membranes (IEM) act as barriers that selectively allow the passage of counter-ions while excluding the co-ions due to the so-called "Donnan exclusion" [11]. Between each couple of membranes, a net spacer is interposed to create the channel for the fluids. The AB-FB is constructed using the plate and frame configuration with the repeating units placed between two end plates. They contain the electrode chambers, which are under a voltage drop that establishes a flow of electrons through the external electrical circuit and of ions through the stack (cations migrate towards the cathode, while the anions move towards the anode). The Electrode Rinse Solution (ERS, for example with Na_2SO_4, or the couple $FeCl_2/FeCl_3$, or hexacyanoferrates) favors the transfer of electrons from the electrodes to the ionic species in solution and vice versa through redox reactions. In the charge phase, the voltage drop is applied by an external electrical generator and holds the BPMs under reverse current bias. This causes the reaction of water dissociation (producing protons and hydroxide ions), which may be promoted by the presence of a catalyst [12], in the transition region of the BPM. As a result of water dissociation and selective ion transport, the charge phase (BMED process) produces an acidic solution and a basic solution, while desalting the salt water. Conversely, in the discharge phase (BMRED process) the "charged" electrolytes generate an electric potential difference over the membranes, especially thanks to the pH gradient over the BPMs, and the circuit is closed externally by an external load. In this condition, the BPMs are under forward current bias, acid/base neutralization occurs in their interlayer, and salt water is produced. Overall, during the charge phase, electricity fed into the battery from an external source is converted into acidic and alkaline solutions, thus storing energy in the form of a pH gradient (Fig. 2a). Conversely, during the discharge phase, the resulting acidic and alkaline solutions are neutralized in a controlled manner to produce electricity again (Fig. 2b).

In recent years, there have been many studies focusing on BMED (i.e., AB-FB charge phase) as a standalone process [13] but relatively few focusing on BMRED [14] (i.e., AB-FB discharge phase). These studies have mainly conducted experimental analyses under several operating conditions (e.g., current and voltage, mean flow velocities, temperature, etc.) and stack sizes (e.g., length, width, number of repeating units, etc.), revealing some relation with the system performance. Only a bi-objective optimisation analysis, with CO_2 productivity and energy demand as objective functions, was performed for the BMED process, specifically for carbon capture applications [15]. However, none of these studies identified a set of conditions that maximise the performance of the BMRED process.

In contrast, several optimisation studies of ElectroDialysis (ED) systems have been performed so far. Chindapan et al. [16] conducted a multi-objective optimisation using the Multi-Objective Genetic Algorithm method (MOGA) with final product concentrations and energy consumption as objective functions. Bian et al. [17] attempted to minimise the overall costs through Particle Swarm Optimization (PSO) [18] from a previous ED model [19]. Guesmi et al. [20] aimed at maximising the boron removal using Response Surface Methodology (RSM). Rohman and Aziz [21] endeavoured to dynamically optimise process time, energy consumption, degree of separation, dilute concentration, and process profit with the orthogonal collocation method, identifying contrasting optimisation requirements. Then, they developed a multi-objective optimisation [22] using a Non-dominated Sorting Genetic Algorithm II (NSGA-II), minimising the energy consumption and maximising the acid concentration. In conventional Reverse ElectroDialysis (RED), Veerman et al. [23] optimised the Net Power Density, the net Energy Density, or their product. Similarly, Long et al. [24] maximised the Net Power Density with the Genetic Algorithm (GA). In another work, the same authors [25] performed a multi-objective optimisation with the NSGA-II algorithm to maximise Net Power Density and Energy Efficiency. Ciofalo et al. [26] also optimised the Net Power Density but using the gradient-ascent algorithm [27]. Faghihi and Jalali [28] used CFD and an artificial neural network for a bi-objective optimisation (Sherwood number ad power number) of RED units.

The story of the AB-FB was started in 1983 by Emrén and Holmstrom [29], who first discussed the possibility of storing energy in the form of acidic and alkaline solutions in fuel cells with BPMs (seven-triplet stack). They proposed the existence of a linear relationship between the electromotive force, the difference in pH across the bipolar membrane layers, and the operating temperature. Several years later, Pretz and Staude [30] assessed the performance of an AB-FB provided with a number of triplets ranging from 2 to 20. Additionally, the concentration range of HCl and NaOH was varied from 0.1 to 1 M; this gave a process efficiency up to 22 %, which is not particularly high due to the water accumulation phenomenon in the BPM junction, especially when operating at high electric currents. In the same year (1998), Zholkovskij et al. [31] conducted experiments with a single-triplet AB-FB tested at very low concentrations of acid and base of 0.03 M obtaining low values of power density and specific energy. More recently, Kim et al. [32] studied a wider range of acid/base concentrations of 0.1 to 0.7 M using a stack with 1 triplet. In this case, the maximum power density achieved was

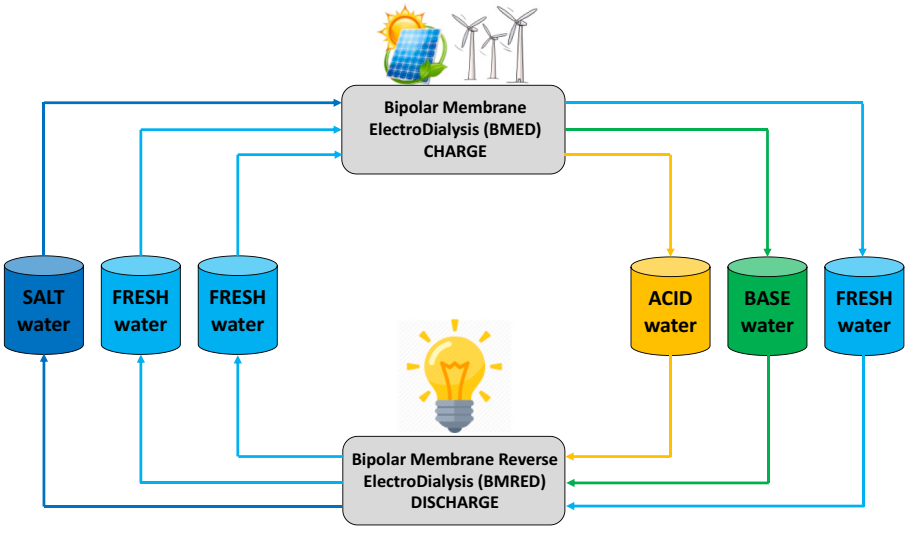

Fig. 1. Scheme of the Acid/Base Flow Battery (from [10]).

2.9 W m^{-2} of total membrane area. Moreover, they related the deviation between the obtained Open Circuit Voltage and the theoretical values (derived from the Nernst equation) to the existence of some detrimental phenomena. These include a low water back-diffusion through the BPM layers, as well as high electrode overvoltages. Van Egmond et al. [9] tested an AB-FB including 1 triplet in the concentration range 0–1 M, performing nine battery cycles. At the highest achieved concentration, the open circuit voltage was 0.83 V, corresponding to an apparent permselectivity of 89 %. Indeed, this study employed Fumatech® membranes, which show high level of performance. In order to prevent membrane delamination (i.e., detachment of the two BPM layers), they limited the maximum discharge current density to 15 A m^{-2}. Compared to prior studies, up to that date, they obtained the highest gross power density (GPD) value of 3.7 W m^{-2}. Other performance metrics were an energy density of 2.9 kWh m^{-3}, and a maximum RTE of 20 %. Xia et al. [33] performed a preliminary study with 1 triplet; subsequently, they studied the behaviour of the AB-FB with multiple triplets, ranging from 5 to 20 [34]. The two studies investigated acid and base concentration ranges 0–1 M [33] and 0.5–1 M [34], respectively. Experiments with 20 triplets exhibited an RTE of ~30 % in a single cycle and a maximum GPD in the discharge phase of 15 W m^{-2} [34]. Despite this value was higher than previous results, it was still affected by detrimental phenomena, such as parasitic currents via manifolds, which occur to a great extent in AB-FB units due to the high conductivity of the acid and alkaline solutions. A GPD of 17 W m^{-2} was achieved with a stack of 10 triplets in one of our recent studies [14], which also estimated minor effects of pumping losses on the net power density (NPD) and an energy density of 10.3 kWh m^{-3} for a complete discharge. These experiments confirmed the presence of shunt currents via manifolds and showed that their effect increases with the number of triplets and the concentration of acid and base achieved at the end of the charge phase. A stack geometry that reduces the cross-sectional area of the manifolds (i.e., collectors and distributors) could be used, but the benefit of reduced parasitic currents should be balanced against (i) the pressure losses and, as a result, (ii) the poorer distribution of the electrolytic solutions in the stack channels. A more effective alternative for reducing parasitic currents is to use fewer triplets by connecting more stacks in blocks. As a result, the battery would be made up of several hydraulically independent stacks, which would reduce the impact of shunt currents [35]. Moreover, the use of multiple battery stages in series can be a strategy to increase the RTE beyond 50 % [35].

The theoretical energy density is proportional to the achieved acid/base concentrations. For example, with concentrations of 1 M HCl and NaOH, the energy density would be 20.8 kWh m^{-3} of acid (or base) solution during the discharge phase. Potentially, with 5 M acid and base concentrations, the theoretical energy density would become 115 kWh m^{-3}. However, membranes should be designed to bear highly acidic and alkaline solutions without damage nor significant drop of performance.

The optimisation of the AB-FB is an essential step to increase the competitiveness of the technology and assess its real potential. Different combinations of operating and design features may significantly affect the performance of the system during both phases (i.e., charge and discharge). These parameters may ultimately have contrasting effects on the performance. The main performance indicators of an AB-FB are the Round Trip Efficiency and the average power density obtained during the discharge. However, it is difficult to find a good compromise. In fact, the discharge power density is a parabolic function of the applied external current. Therefore, it may be maximised when higher ohmic losses lead to a lower RTE. Moreover, the risk of BPM delamination may limit the safe discharge current to values that do not provide the maximum power density. Finally, pumping power may play an important role in the discharge phase. Thus, power losses must be limited and the search for optimal conditions is not straightforward at all.

The aim of this study was to conduct, for the first time, a bi-objective optimisation of the AB-FB utilising the epsilon-constraint method targeting the maximum net Round Trip Efficiency and the maximum average net discharge power density. The gPROMS Model Builder optimisation tool was used to find optimal solutions, and the dynamic behaviour and the performance of the AB-FB were predicted by a multi-scale model previously developed by our group [10,36,37]. Several scenarios were simulated by letting two to eight operating and design decision variables to vary contemporaneously, determining the best solutions in the form of Pareto frontiers and providing a broad picture of the AB-FB technology potential.

2. Mathematical modelling

The mathematical model was initially developed in 2020 in our previous work [10]. Then the model was modified by integrating ad-hoc equations to accurately predict the behaviour of the bipolar membrane during the charging [37] and discharging phases [36]. Our previous works have highlighted that electro-membrane processes can be accurately simulated, while maintaining an appropriate computational burden, by integrating calculations of non-ideal phenomena (e.g., concentration polarisation, parasitic currents via manifolds) and pressure losses. The simulation tool developed in our previous study is semi-empirical, as it describes the process through phenomenological equations that contain membrane parameters whose values are obtained experimentally [10]. Phenomenological equations are used for predicting water and ion transport across both monopolar and bipolar membranes. The empirical information that must be provided to the model concerns membrane properties such as electrical resistances and ion

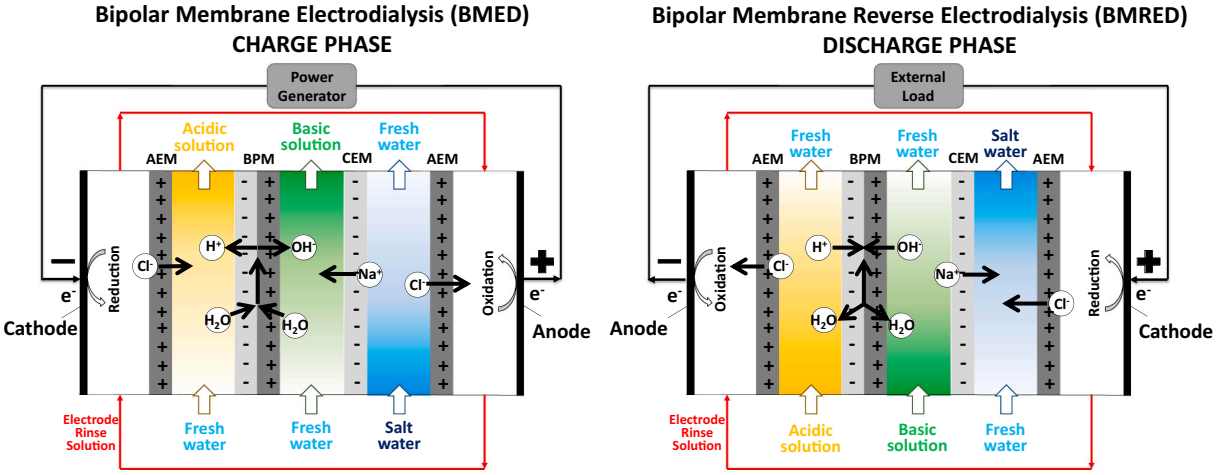

Fig. 2. Illustration of the Acid/Base Flow Battery phases: a) charge and b) discharge.

diffusivities. NaCl, HCl and NaOH are the electrolytes simulated for the salt, acid, and base, respectively.

The hierarchical structure of the multi-scale model used for the present optimisation study is the same as in previous works on BMED [37], BMRED [36] and AB-FB [10]. The basic model presented in [10] was taken to simulate most scales, except for the bipolar membrane level, which was simulated as in [36,37] for the charge phase and discharge phase, respectively.

The BPM model predicts the value of the limiting current of salt (NaCl in this case) migrating across the bipolar membrane layers. Furthermore, this model takes into consideration that the membrane is not completely perm-selective to protons in the CEL and to hydroxide ions in the AEL and, thus, that the transport numbers of these ions in the BPM layers may vary depending on the concentration of the other ions in the solution.

For the complete description of the model, see the Supplementary Information.

Note that the present optimisation study was performed with simulations of the AB-FB working with recirculation of the electrolyte solutions into the feed tanks, each assumed with perfect mixing.

The optimisation simulations were carried out in the gPROMS Model Builder® platform.

2.1. Optimisation method and figures of merit

The optimisation was conducted with two objective functions, i.e., maximising the net Round Trip Efficiency (RTE_{net}) and maximising the average Net Power Density per unit membrane area produced during the discharge phase ($\overline{NPD_d}$). The former quantity clearly measures the conversion efficiency of the available energy. Net values of energy or power include the requirements for pumping the electrolyte solutions through the stack. The Net Power Density (NPD) was calculated as,

$$NPD = GPD \pm PPD \tag{1}$$

where GPD is the Gross Power Density and PPD is the Pumping Power Density, all measured in W m^{-2} of total membrane area. In Eq. (1) the sign + applies in the charge phase, while the sign – applies in the discharge phase.

The average Net Power Density in the discharge phase ($\overline{NPD_d}$) is defined as follows,

$$\overline{NPD_d} = \frac{\int_0^{t_d} NPD_d \, dt}{t_d} \tag{2}$$

where t_d is the discharge time.

The net Round Trip Efficiency is defined as follows,

$$RTE_{net} = \frac{\int_0^{t_d} (GPD_d - PPD_d) dt}{\int_0^{t_c} (GPD_c + PPD_c) dt} \tag{3}$$

in which t_c is the charge time.

The theoretical and actual Net discharge Energy Densities per unit volume of a reference solution (the acid solution was chosen in this study) are given by Eqs. (4) and (5) respectively:

$$NED_{v,th} = \frac{F}{3.6 \bullet 10^6} \int_{10^{-4}}^{C_{target,c}} EMF \bullet dC_{a,HCl} \tag{4}$$

$$NED_v = \frac{3 \, N \, b \, L \int_0^{t_d} (GPD_d - PPD_d) \, dt}{3.6 \bullet 10^6 \bullet V_{t,a}} \tag{5}$$

where F is the Faraday constant (i.e., 96,485C mol^{-1}), EMF is the Nernst potential, $C_{target,c}$ is the target concentration of the charge phase, $C_{a,HCl}$ is the HCl concentration in the acid tank, N is the number of triplets, b is the spacer width, L is the spacer length, and $V_{t,a}$ is the acid solution volume.

The efficiency of the discharge phase is the ratio between the actual and theoretical net energy density. It is given by,

$$Discharge\ efficiency = \frac{NED_v}{NED_{v,th}} \tag{6}$$

Each optimisation problem consists of a single round-trip cycle, which begins with the charge phase, followed by the discharge phase. Each battery cycle is carried out by imposing that the initial concentration of HCl in the acidic solution is coincident to the final (target) concentration of HCl of the discharge phase ($C_{target,d}$) as follows:

$$C_{a,HCl,target,d} = C_{t,HCl,out,a} \tag{7}$$

Therefore, each cycle begins and ends at the same acid concentration and (approximately) the same base concentration. The acid concentration targets are representative of the maximum state of charge of the battery. For example, the state of charge may be 0 % when the concentration reaches 0 M HCl and 100 % when it reaches 1 M HCl.

A multi-objective optimisation problem may be generally defined as the minimisation (or the maximisation) of a vector of objective functions [38]:

$$max\{f(\boldsymbol{x})\} \leftrightarrow min\{-f(\boldsymbol{x})\} \tag{8}$$

$$f(\boldsymbol{x}) = [f_1(\boldsymbol{x}), f_2(\boldsymbol{x}), \ldots, f_m(\boldsymbol{x})]^T \tag{9}$$

$$g_i(x) \leq 0 \ (i = 1, 2, \ldots, p) \tag{10}$$

$$h_k(x) = 0 \ (k = 1, 2, \ldots, q) \tag{11}$$

$$x_i^{min} \leq x_i \leq x_i^{max} \ (i = 1, 2, \ldots, n) \tag{12}$$

where f is the objective functions vector, $\boldsymbol{x}$ is the vector of the decision variables falling within the interval between the lower and upper limits as in Eq. (12). Eqs. (10) and (11) denote p- inequalities and q-equalities constraints.

In this work, bi-objective optimisation problems were solved by using the optimisation tool of gPROMS Model Builder®. Since this software allows only to solve single-objective optimisation problems, the two-objective optimisation was performed by using the ε-constraint method. This method was proposed in 1971 by Haimes et al. [39]. It allows using a single-objective function, transforming the other functions in inequality constraints with its upper (or lower) bounds [40]. In the present work, the bi-objective optimisation functions are the maximisation of RTE_{net} and of $\overline{NPD_d}$.

Importantly, each single-objective problem entails pursuing the objective function (maximisation) of one quantity (RTE_{net}) for a series of constrained values of the other quantity ($\overline{NPD_d}$). Therefore, the problem can be formalised as follows:

$$\text{Objective}: Max\ RTE_{net}(\boldsymbol{x}) \tag{13}$$

$$\text{Subject to}: \overline{NPD_d}(\boldsymbol{x}) \geq \varepsilon \tag{14}$$

$$g(\boldsymbol{x}) \leq 0 \tag{15}$$

$$h(\boldsymbol{x}) = 0 \tag{16}$$

The main results of the present optimisation study were expressed in the form of Pareto optimal fronts, each consisting of a curve of best trade-off points between the two chosen objective functions (optimal among the feasible solutions [38]). Any point of the Pareto frontier represents an optimal solution that maximises RTE_{net} under a constraint on the value of $\overline{NPD_d}$ and vice versa. The region below the Pareto set is that of feasible but non-optimal solutions, while the region above it regards unfeasible solutions.

The decision variables were of two types: operating and design variables (Table 1). The reference value of any parameter was fixed in

Table 1
List of the decision variables with their reference values and bounds.

Variable name	Symbol, unit	Lower bound	Upper bound	Reference
Operating variables				
Charge current density	i_c, A m^{-2}	30	500	100
Discharge current density	i_d, A m^{-2}	30	200	30
Charge mean flow velocity	$u_{ch,sol,c}$, cm s^{-1}	0.5	5	1
Discharge mean flow velocity	$u_{ch,sol,d}$, cm s^{-1}	0.5	5	1
Charge target concentration	$C_{a,HCl,target,c}$, mol m^{-3}	500	1000	1000
Discharge target concentration	$C_{a,HCl,target,d}$, mol m^{-3}	50	200	50
Design variables				
Spacer length	L, cm	5	200	44
Spacer thickness	d_{sol}, μm	50	1000	500

simulated scenarios where that parameter was not considered as a decision variable. In the case of the charge target concentration, the reference value (1000 mol m^{-3}) was taken as upper bound to maintain the simulations in a range of concentrations where the membrane selectivity is not impaired, and the transport properties can be considered constant.

Four different scenarios (A to D) were investigated to evaluate the separate effects of the decision variables on optimal solutions. These scenarios include an initial ($t = 0$) solutions' volume ratio (i.e., $V_{t,a} : V_{t,b} : V_{t,s}$) of 1:1:6 to decrease the NaCl concentration variations in the salt channels and thus prevent the complete depletion of NaCl during battery charging. An additional scenario (E) was simulated by reducing the salt solution volume, and thus changing the solutions' volume ratio to 1:1:1 instead of 1:1:6. In this case, the initial NaCl concentration in the salt solution ($C_{t,NaCl,s}$) was increased from 500 mol m^{-3} to 1000 mol m^{-3} to guarantee the presence of a sufficient quantity of salt to charge the acid and base solutions. Finally, a scenario of improved membrane properties (scenario F) was simulated to explore the potential enhancement in the battery performance thanks to a possible future improvement of its key elements. The improved membranes were simulated assuming electrical resistance, ion diffusivities and water permeability at 50 % of the reference values (pertaining the membranes simulated in all other scenarios) (see Table 3). The six simulated scenarios are described in Table 2.

Table 2
List of the optimisation scenarios.

Scenario	Decision variables	Initial $C_{t,NaCl,s}$, mol m^{-3}	Initial $V_{t,a} : V_{t,b} : V_{t,s}$	Membrane properties
A	i_c, i_d	250	1:1:6	Reference
B	i_c, i_d, $u_{ch,c}$, $u_{ch,d}$	250	1:1:6	Reference
C	i_c, i_d, $u_{ch,c}$, $u_{ch,d}$, $C_{a,HCl,target,c}$, $C_{a,HCl,target,d}$	250	1:1:6	Reference
D	i_c, i_d, $u_{ch,c}$, $u_{ch,d}$, $C_{a,HCl,target,c}$, $C_{a,HCl,target,d}$, L, d_{sol}	250	1:1:6	Reference
E	i_c, i_d, $u_{ch,c}$, $u_{ch,d}$, $C_{a,HCl,target,c}$, $C_{a,HCl,target,d}$, L, d_{sol}	1000	1:1:1	Reference
F	i_c, i_d, $u_{ch,c}$, $u_{ch,d}$, $C_{a,HCl,target,c}$, $C_{a,HCl,target,d}$, L, d_{sol}	250	1:1:6	Improved[1]

[1] By halving electrical resistances, ion diffusivities and water permeability of the IEMs (see Table 3).

Table 3 reports the reference values of the membrane properties, while Table 4 reports the parameters adopted for all simulations. A woven spacer with 90° angled filaments, a pitch-to-height ratio of 2, and a flow attack angle of 45° were used in the simulations of the AB-FB described in this paper.

The AB-FB reference design simulated in this work is the one developed in the framework of the EU-funded BAoBaB project [35].

3. Results and discussion

In this section, the bi-objective optimisation results are presented and discussed in detail.

3.1. Pareto frontiers

In this section, the optimisation results are presented. The Pareto frontiers of all the simulated scenarios are reported in Fig. 3, which provides a clear picture of the battery potential and of the significance of the decision and scenario variables. All curves are monotonically decreasing with concavity downwards.

The Pareto curve for scenario A (where the charge and discharge current densities are the only decision variables) shows a maximum of RTE_{net} of 50.6 %, which corresponds to the minimum of the constrained $\overline{NPD_d}$ equal to 5.78 W m^{-2}. At the opposite side of the frontier, the maximum value of constrained $\overline{NPD_d}$, equal to 13.0 W m^{-2}, provides an RTE_{net} of 40.6 %.

Along with the two decision variables from scenario A (charge and discharge current densities), scenario B includes the mean channel flow velocities in the two battery phases. Notably, using mean channel flow velocities as decision variables indirectly influences the volumetric flow rates of the electrolyte solutions fed into the battery. The resulting Pareto curve is by 3/4 almost overlapped to that of scenario A but extends on the right side towards higher values of $\overline{NPD_d}$ (up to 14.5 W m^{-2}, with an associated RTE_{net} reduced to 32.1 %).

In scenario C, the target concentrations of charge and discharge are added as decision variables. The difference in acid concentration between the beginning and the end of discharge could range from a minimum of 300 mol m^{-3} (i.e., the difference between the lower bound charge target concentration and the upper bound discharge target concentration) to a maximum of 950 mol m^{-3} (i.e., the difference between the upper bound charge target concentration and the lower bound discharge target concentration). The latter value corresponds to that fixed in scenario A and B. Overall, the Pareto frontier C is characterised by a wider range of power density and by higher values of RTE_{net}. This shows that operating the AB-FB with shorter concentration jumps between 0 and 100 % state of charge can yield significant improvements in the optimal solutions. Moreover, the Pareto frontier of scenario C

Table 3
Reference values for membrane properties (from [35]).

		AEM	CEM	BPM	
				AEL	CEL
Thickness (d_m)	μm	75	75	60	60
Areal resistance (R_m)	Ω cm^2	4	3.5	2.5	2.5
Water permeability (L_p)	ml bar^{-1} h^{-1} m^{-2}	8	8	–	–
H^+ diffusivity ($D_{H,m}$)	m^2 s^{-1}	2.0E-11	0.7E-11	2.0E-11	0.7E-11
Na^+ diffusivity ($D_{Na,m}$)	m^2 s^{-1}	1.6E-11	0.5E-11	1.6E-11	0.5E-11
Cl^- diffusivity ($D_{Cl,m}$)	m^2 s^{-1}	1.7E-11	0.6E-11	1.7E-11	0.6E-11
OH^- diffusivity ($D_{OH,m}$)	m^2 s^{-1}	1.9E-11	0.6E-11	1.9E-10	0.6E-11
Fixed charge density (X_m)	mol m^{-3}	5000	5000	5000	5000

Table 4
Fixed parameters.

Geometrical features		
Spacer width (b)	cm	47.6
Spacer type	–	Woven
Spacer pitch-to-height ratio	–	2
Spacer flow attack angle	–	45°
N° spacer holes for manifolds (N_{holes})	–	1
Spacer hole area for manifolds	mm^2	400
N° triplets (N)	–	10

Process conditions		
Initial NaCl concentration in the acid solution ($C_{t,HCl,out,a}$)	mol m^{-3}	250
Initial volume of the acid solution ($V_{t,a}$)	l	10
Initial NaCl concentration in the base solution ($C_{t,NaCl,out,b}$)	mol m^{-3}	250
Initial volume of the base solution ($V_{t,b}$)	l	10
Initial NaCl concentration in the salt solution ($C_{t,NaCl,out,s}$)	mol m^{-3}	500
Blank resistance (R_{bl})	Ω cm^2	12

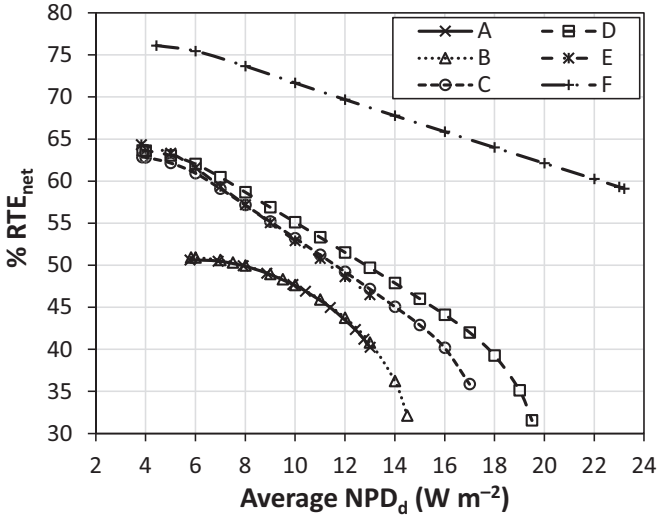

Fig. 3. Pareto frontier of net RTE as a function of the $\overline{NPD_d}$ for all the simulated scenarios.

exhibits a long linear tract apart from the regions very close to the extreme optimal and feasible points. The maximum RTE_{net} (62.9 %) obtained in scenario C is >10 percentage points higher than that of scenario A and B, but at the expense of a further reduction of the corresponding $\overline{NPD_d}$ (dropped to 4.13 W m^{-2}). Moreover, the concentration at which the maximum RTE_{net} is found corresponds to 0.6 M HCl; thus, the effect of a variation of the lower limit of $C_{a,HCl,target,c}$ is included in another scenario. Specifically, for scenario D, the lower limit of the charge concentration is fixed at 0.5 M.

Two design features are added in scenario D, namely spacer thickness and length. By comparing scenarios C and D, it can be drawn that when adding the design variables, only minor improvements (up to about 12 % in relative terms) are predicted. Furthermore, the two curves C and D differ only slightly on the left side of the Pareto front. Indeed, scenario D results in a 0.8 % increase in RTE (in absolute value). As the $\overline{NPD_d}$ increases, the difference between the two curves grows. Specifically, the maximum $\overline{NPD_d}$ in scenario D is 19.5 W m^{-2}, thus resulting 15 % higher compared to the maximum value for scenario C.

Scenario E, devised to investigate the effect of a reduced volume of the salt solution by including all the decision variables, shows similar optimal results compared to scenario D. The most evident difference that distinguishes the two solutions' volume ratios $V_{t,a} : V_{t,b} : V_{t,s}$ of 1:1:1 (scenario E) and 1:1:6 (scenario D) is that in the former case the Pareto frontier extends to a significantly lower maximum of $\overline{NPD_d}$ (13 W m^{-2}). Indeed, a convergence failure of the optimisation tool occurred at higher constrained values of power density due to an excessive reduction of the outlet NaCl concentration from the stack, particularly at the end of the charge phase. Higher values of initial concentration of salt may avoid this issue but would certainly lead the optimal solutions to lower values of RTE_{net}, as also shown by the slope of the Pareto curve E on the side of the maximum power density.

Finally, the Pareto frontier obtained with improved membrane properties provides a possible future scenario for the AB-FB technology. Improved membranes (scenario F) may lead to a significantly enhanced performance, as highlighted by a comparison taking scenario D (current membranes) as a baseline. It is important to note that the scenario F curve results to be translated upwards and elongated to the right side as $\overline{NPD_d}$ values increase. In particular, higher average values over the Pareto front for both RTE_{net} and $\overline{NPD_d}$ are obtained. Overall, the Pareto frontier F lies almost on a straight line between the point of maximum RTE_{net} (4.43 W m^{-2}, 76.1 %) and the point of maximum $\overline{NPD_d}$ (23.2 W m^{-2}, 59.1 %).

By considering that the maximum values of RTE and GPD reported in previous studies conducted with lab-scale stacks (see Introduction) were ~30 % and 15–17 W m^{-2}, respectively, the present results (Fig. 3) clearly show that the performance of the AB-FB can be significantly improved by adequately designing and operating it. Note that the experimental values of maximum GPD are quite high even compared with the optimal values of average NPD found in this study. However, the experimental values are gross, not net (i.e., they do not take into account pumping losses). More importantly, those GPD values were recorded in once-through experiments. Hence, a reduction of average power density is expected across a whole discharge. Therefore, optimised systems present a great room for improvement in terms of both efficiency and power density.

3.2. Optimal decision variables

The optimal values predicted for the decision variables are reported in Fig. 4 as functions of $\overline{NPD_d}$ for one selected scenario, which is scenario D. Although interpreting the combined effects of eight decision variables is complex, some interesting points for discussion regarding optimal solutions can be drawn.

The predicted values of current densities (Fig. 4a) show an increasing trend with the $\overline{NPD_d}$, that means a decreasing trend with the RTE_{net}. Indeed, as the $\overline{NPD_d}$ increases, the RTE_{net} in the Pareto curves (shown in Fig. 3) shows a monotone decreasing trend. The optimal current densities of charge and discharge were 50–220 A m^{-2} and 30–190 A m^{-2}, respectively. The minimum values correspond to the lower bounds (see Table 1), the maximum discharge current density is close to its upper bound (200 A m^{-2}), and the maximum discharge current density is far from its upper bound (500 A m^{-2}). At lower current densities, the resulting voltage efficiency is higher as the external voltage tends towards the open circuit condition in both charge and discharge phases. On the other hand, a higher current density of discharge provides higher values $\overline{NPD_d}$, probably indicating the approaching of the maximum point in the power-current curve. Indeed, previous studies showed values of current densities above 100 A m^{-2} at the condition of maximum power density [14]. Higher discharge power densities required also higher current densities in the charge phase to obtain an optimal solution, which lead to higher values of the electromotive force (as indicated by the higher target concentration of charge reported in Fig. 4c).

The mean flow velocities across the Pareto frontier (Fig. 4b) span from 0.68 to 1.2 cm s^{-1} for the charge and from 0.55 to 1.2 cm s^{-1} for the discharge. Therefore, the optimal velocities vary in a range narrower than that allowed by the lower and upper bounds (0.5 and 5 cm s^{-1}) and

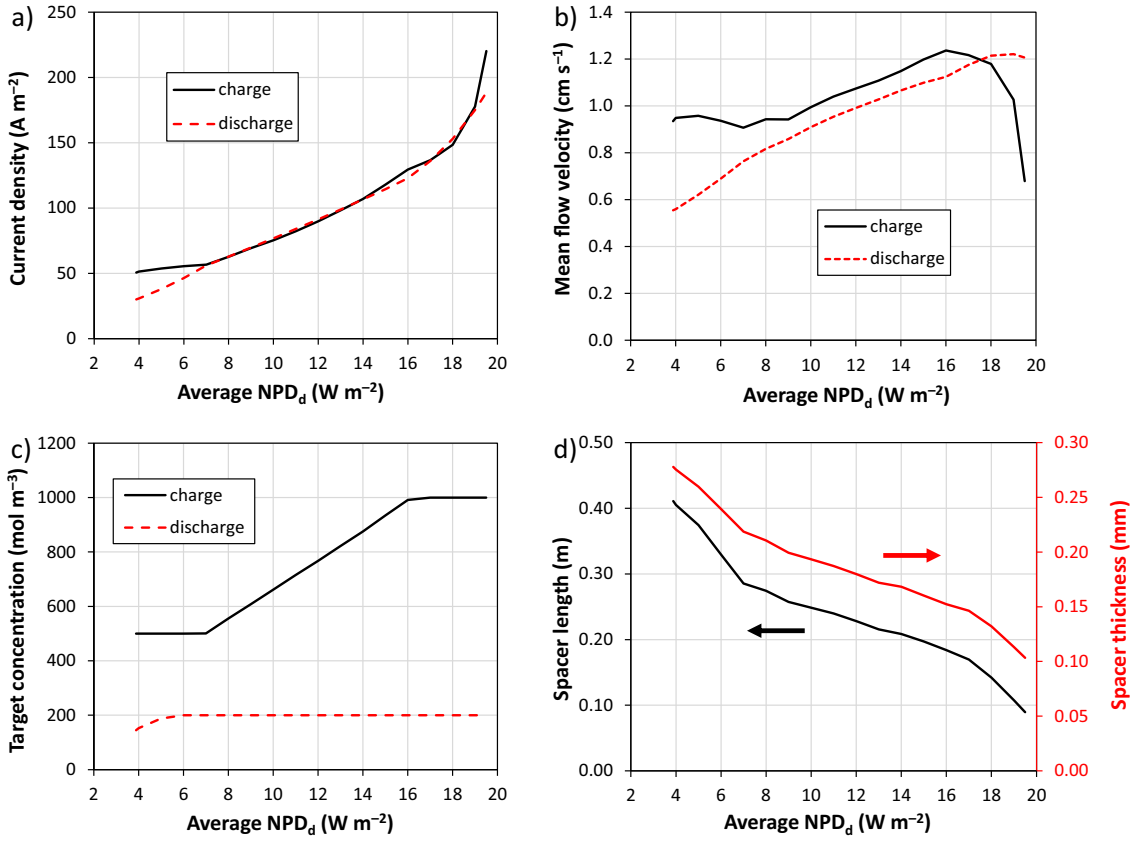

Fig. 4. Optimal values of the decision variables as functions of the $\overline{NPD_d}$ for scenario D. a) i_c and i_d, b) $u_{ch,c}$ and $u_{ch,d}$, c) $C_{a,HCltarget,c}$ and $C_{a,HCl,target,d}$, and d) L and d_m.

cover the lower part of it. The charge and discharge phases exhibit a similar behaviour and an increasing trend of the optimal velocity as a function of $\overline{NPD_d}$, apart from the last tract of the curve (especially for the charge phase, roughly corresponding to a sudden increase in current density). The flow velocity influences the pumping power consumption in a complex pattern involving the design variables, i.e., the spacer length and thickness. However, calculating the difference between the gross and net RTE in the range of the Pareto curve reveals that the pumping power affects the optimal solutions almost negligibly, e.g., resulting only in a 1 % reduction in RTE on average. Other effects of the fluid velocity regard the operating time (and, indirectly, the current efficiency related to non-ideal transport phenomena) and the concentration polarisation. However, these features depend also on the other variables of the problem.

Concerning the target concentration profiles (Fig. 4c), apart from a short stretch, the discharge target concentration shows a constant profile against the $\overline{NPD_d}$ lying on the upper limit of $C_{target,d}$ (200 mol m^{-3}). In contrast, the optimal $C_{target,c}$ has a great variation, covering the whole interval assigned to the decision variable. In particular, $C_{target,c}$ is the lowest (500 mol m^{-3}) at low $\overline{NPD_d}$ values of 4–7 W m^{-2} (corresponding to higher RTE_{net} values, see Fig. 3), and then increases up to the highest value (1000 mol m^{-3}) at high $\overline{NPD_d}$ values of 16–19.5 W m^{-2}. This confirms that the maximisation of RTE_{net}, corresponding to the minimum $\overline{NPD_d}$, is achieved by lower concentration jumps between 0 and 100 % state of charge. As demonstrated in Fig. 4c, higher or lower limits of the charge target concentrations could be beneficial for reaching higher values of the objective functions. However, these may not be of practical interest in the search of the optimal working point, which will require some balance between the two objective functions. Moreover, current ion-exchange membranes cannot be used with high acid and base concentrations due to unsuitable properties of selectivity. On the other hand, too low acid and base concentrations would decrease the electromotive force and thus the obtainable energy density.

Finally, spacer length and thickness (Fig. 4d) show both a similar (at least qualitatively) decreasing trend with $\overline{NPD_d}$. The range of the optimal stack lengths is 9–41 cm and is far from the assigned upper limit of 200 cm. This means that long stacks (more than ~40 cm) are not beneficial for maximising our objective functions because stacks with channels longer than ~40 cm would fall outside the Pareto frontier. Within the optimal range, shorter stacks (9–41 cm) are suitable for optimising $\overline{NPD_d}$ due to the increase in average electric potential. On the other hand, longer stacks are preferable to maximise RTE_{net} despite lower $\overline{NPD_d}$ values due to the reduction of parasitic currents via manifolds combined with lower electrical resistance. The optimal spacer thickness decreases from ~280 μm to 100 μm, despite the range of possible values being significantly higher (i.e., 50–1000 μm). Therefore, thin channels are optimal for the battery performance. Thicker spacers probably contribute to reduce parasitic currents, thus being optimal to maximise RTE_{net} as depicted in Fig. 4d; thinner ones reduce the electrical resistance, resulting optimal to maximise $\overline{NPD_d}$, which is less affected by pumping power, as mentioned above. It is worth noting that the inclusion of mean channel flow velocities and spacer thickness as decision variables results in an indirect variation of the volumetric flow rate of the electrolyte solutions. The optimal values of the volumetric flow rates of the inlet streams vary along the Pareto curve within the range of 12–45 L h^{-1} in the charge phase and 21–31 L h^{-1} in the discharge phase.

3.3. Energy density

Fig. 5 shows the theoretical and actual energy densities at the extreme points of the Pareto frontier of all the simulated scenarios.

In scenario A the theoretical energy density at the maximum RTE is

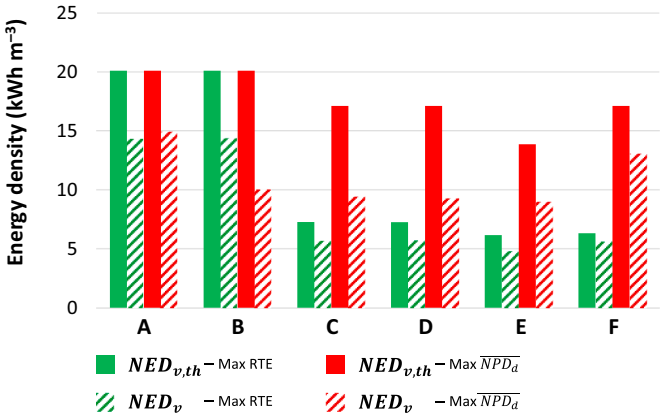

Fig. 5. Theoretical and actual energy density at the two extreme points of the Pareto curve representing the single-objective optimal conditions of maximum net RTE and maximum $\overline{NPD_d}$ in discharge.

20.1 kWh m^{-3}, and this value is always equal across the Pareto set because it depends only on the target concentration of charge (Eq. (4)), which is fixed at 1 M HCl (together with the discharge target concentration at 0.05 M HCl). The actual energy density is lower due to non-ideal phenomena that occur during the battery discharge operation. It is affected also by the target concentration of the discharge, which is fixed at 50 mol m^{-3}. In particular, at the maximum net RTE and maximum $\overline{NPD_d}$, the discharge efficiency (see Eq. (6)) in scenario A is 71 % and 74 %, respectively.

In scenario B the theoretical energy density is the same as in scenario A. However, the actual energy density is similar in the two scenarios only when maximising RTE_{net}, while it is significantly reduced in scenario B when maximising the $\overline{NPD_d}$. These features reflect the similarities (left side) and differences (right side) between the Pareto frontiers of the two scenarios described above.

In scenario C, by letting the target concentrations to vary, both the theoretical and actual energy density are affected and vary across the optimal solutions. At the point of maximum RTE_{net}, the theoretical energy density is about 1/3 compared with scenario A and B, indicating that the single objective function on the RTE_{net} is achieved with a lower optimal target concentration of charge. The actual energy density is lower as well (5.68 kWh m^{-3}), but corresponds to a higher discharge efficiency (78.2 %). At the opposite extreme, optimal point of maximum $\overline{NPD_d}$, the theoretical energy density (~17.1 kWh m^{-3}) is closer to that of scenario A and B (meaning that the target concentration of charge is close to 1000 mol m^{-3}), and the associated discharge efficiency is ~55 %.

In scenario D, the energy density is practically unaffected by the design variables, at least at the two extreme optimal points. Additionally, comparing scenarios E and D all energy density values are slightly reduced by the higher salt concentration.

Furthermore, the main difference found when simulating improved membranes (scenario F) compared to commercial membranes (scenario D) is the higher actual energy density values, especially in the condition of maximum $\overline{NPD_d}$. As a result, higher discharge efficiency is obtained, reaching values of 89 % at maximum RTE_{net} and 76 % at maximum $\overline{NPD_d}$. These results, along with the Pareto curve, demonstrate the significant improvements that can be obtained with reduced electrical resistance and increased permselectivity. Indeed, when compared to the reference scenario, improved membranes increased the RTE_{net} by an average of 13 percentage points and $\overline{NPD_d}$ by 2 W m^{-2} (Fig. 3), while discharge efficiency increased by 16 percentage points on average given by the largest fraction of NED theoretical harvested (Fig. 5).

3.4. Performance comparison and criticality analysis of commercial batteries

There are several energy storage systems available in the battery market. The ranges of RTE and of Power Density per Unit Volume of the battery (PDUV) (in the discharge phase) [41] of these technologies taken from the literature [41–45] are depicted in the bubble plot of Fig. 6.

Although the RTE ranges are relatively similar among the technologies (30 %–100 % overall, 60 %–90 % in most cases), the PDUV spans across several orders of magnitude, from 0.01 W L^{-1} to 120,000 W L^{-1}, as shown in the semi-logarithmic plot. According to the results obtained in this study, optimal solutions of the AB-FB show values of RTE from ~30 % to 75 %, and values of PDUV in the range of ~20–2100 W L^{-1}. This means that the AB-FB has middle-low performance in terms of RTE, while it has middle-high performance in terms of PDUV.

Depending on the technology adopted, the energy stored by the battery can be discharged over time periods ranging from seconds to months. In the case of the AB-FB, the time period of discharge is in the order of hours, making this technology ideally suited for stationary energy storage applications, such as for residential power demand or apartment complexes, but also for peak-shaving applications, thus enabling grid stabilisation.

Beyond purely technical features (e.g., RTE or PDUV), other criteria should be considered for the evaluation of battery technologies for large-scale commercialisation. In the perspective of sustainability (economic, environmental, social and political) one crucial aspect is the "material criticality", which is a measure of access to a specific raw material and of the potential impact of a hypothetical shortage. The EU Commission has developed a method for determining material criticality based on evaluating two indices: Supply Risk (SR) and Economic Importance (EI). These two indices are evaluated using several factors. Specifically, the factors that determine the Supply Risk index are: i) substitutability (i.e., a measure of the difficulty of substituting the material, scored and weighted across all applications); ii) end-of-life recycling rates (i.e., a measure of the produced metal products from End-of-Life); iii) country concentration of the material; and iv) governance-related factors. The Economic Importance index is calculated by determining the proportion of each material end-use associated with mega-industrial sectors at the EU level. These proportions are then combined with the Gross Value Added (GVA) of the mega industries and the Gross Domestic Product (GDP) of the EU, ultimately defining a material's overall economic importance. The European Commission recently designated materials with a SR index >1 and an EI index >2.8 as critical [47]. Fig. 7 reports the SR and EI indices for the main materials used in the battery technologies depicted in Fig. 6 [47–59].

As shown in Fig. 7, most of the existent battery technologies employ one or more materials whose values of SR and/or EI exceed the limit. The AB-FB is not depicted in Fig. 7 since the polymer of the ion exchange membranes is the major material in the AB-FB battery, and it is not subject to the criticality assessment because it is not significantly influenced by supply disruptions or economic dependency. Furthermore, the electrodes represent another component of the AB-FB, and they can be built of any carbon source, resulting in a low level of criticality.

Overall, the AB-FB provides performance comparable to that of the leading technologies currently on the market, but with the added benefits of low criticality of the materials used for its production. Moreover, it uses non-hazardous materials, thus being a good candidate for future sustainable applications.

Regarding economic aspects, although the AB-FB requires a large membrane area, it has the potential to be competitive with other electrical energy storage systems, such as the vanadium redox flow battery, and other systems (lead-acid or organic flow batteries). Indeed, the AB-FB benefits from a low cost of the energy subsystem (electrolyte solutions and associated components) [35,60]. However, much effort is still required to address the challenge of developing new membranes with

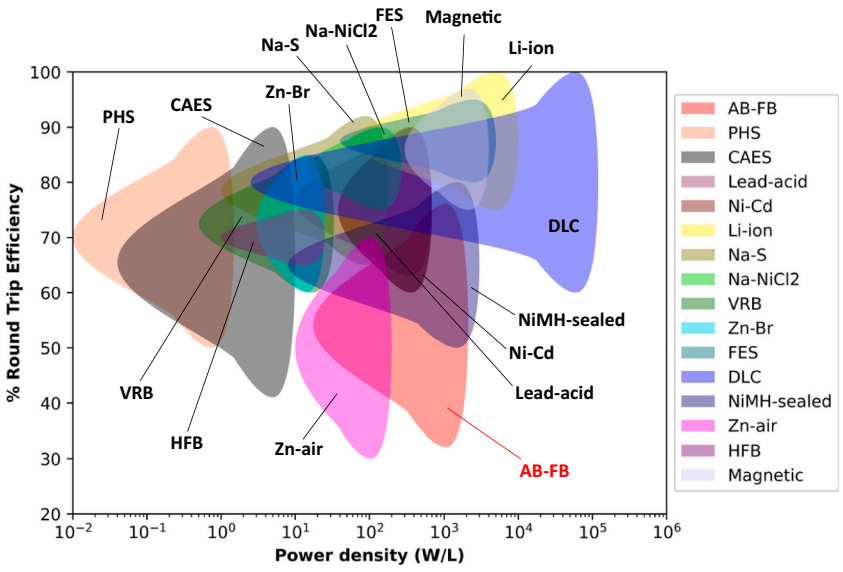

Fig. 6. Comparison of batteries' performance in terms of Round Trip Efficiency and Power Density per Unit Volume [42–46]. Storage systems: Acid-Base Flow Battery (AB-FB); Pumped Hydro Storage (PHS); Compressed-Air Energy Storage (CAES); Lead-acid battery (Lead-acid); Nickel-Cadmium battery (Ni-Cd); Lithium-ion battery (Li-ion); Sodium-sulfur battery (Na-S); Sodium-Nickel-Chloride battery (Na-NiCl2); Vanadium Redox Flow Battery (VRB); Zinc-Bromine battery (Zn-Br); Flywheel Energy Storage (FES); Double Layers Capacitor (DLC); Nickel-metal hydride battery (NiMH-sealed); Zinc-air battery (Zn-air); Hybrid Flow Battery (HFB); Magnetic battery (Magnetic).

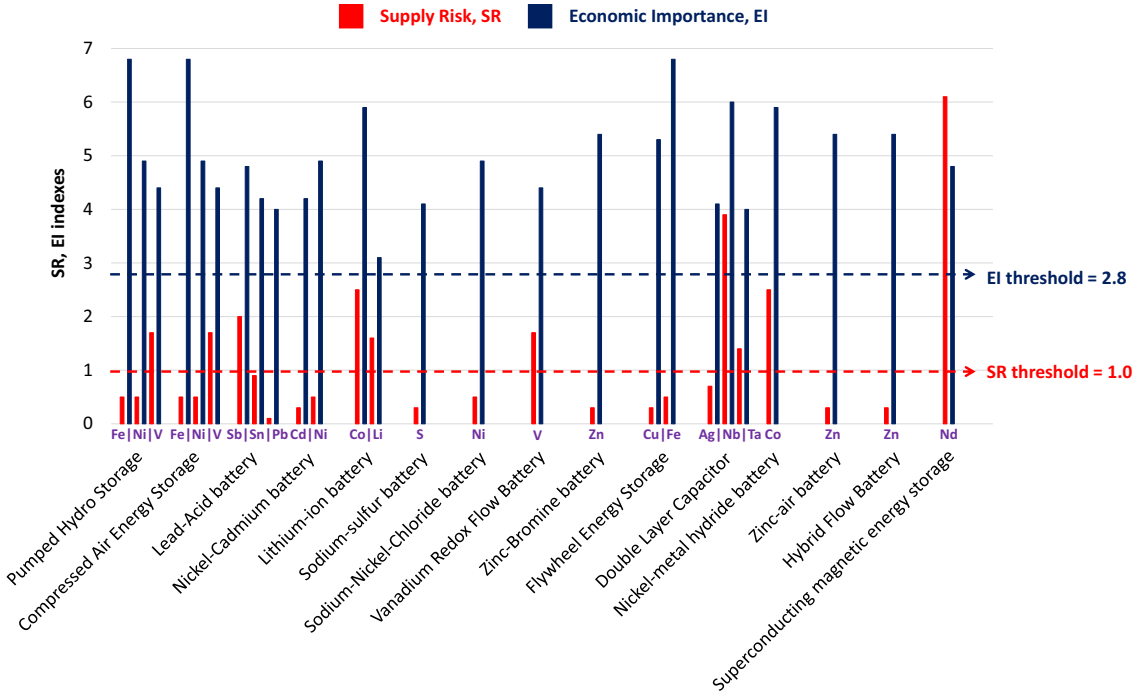

Fig. 7. Supply Risk (SR) and Economic Importance (EI) of batteries' technology-critical elements. Elements per each battery are indicated in bold purple. (For interpretation of the references to color in this figure legend, the reader is referred to the web version of this article.)

low cost and high performance, which are essential for a successful techno-economic profile of the AB-FB.

4. Conclusions

In this work, a previously developed mathematical model for the AB-FB was improved by incorporating models that predict the behaviour of the bipolar membrane during the charge and discharge phases. After that, the mathematical tool was used to determine the best design and operating conditions for maximising net Round Trip Efficiency and average net discharge power density in a closed-loop configuration. A bi-objective optimisation was performed utilising the ε-constraint method, with up to 8 decision variables and for different process scenarios.

The results show that operating with shorter concentration jumps between 0 and 100 % state of charge may improve Round Trip Efficiency significantly, whereas introducing design parameters as decision variables has little effect on the battery performance. When commercial membranes currently available are used, optimised operating conditions and design features may be chosen to maximise the net Round Trip Efficiency up to a value of 64 %, corresponding to an average discharge net power density of ~4 W m^{-2}. On the other hand, by constraining the $\overline{NPD_d}$ at 19.5 W m^{-2}, the Pareto set gave an RTE_{net} of ~32 %. Considering a future scenario with improved membrane properties, the potential maximum RTE_{net} could be 76.2 % when the constraint $\overline{NPD_d}$ is 4.4 W m^{-2}. These results, together with the whole Pareto curve,

demonstrate the significant benefits that may be obtained with lower electrical resistance and greater permselectivity. By constraining the $\overline{NPD_d}$ at the maximum value of 23.2 W m^{-2}, the resulting RTE$_{net}$ was 59.1 %.

A performance analysis reveals that the RTE$_{net}$ and Power density (per unit volume of the battery) of the AB-FB is not significantly different from the average values of other batteries. However, most of the materials used in the construction of the other batteries have Supply Risk (SR) or Economic Importance (EI) indexes higher than the EU commission's threshold limits. In contrast, the primary components of the AB-FB are the polymers that constitute the membranes and spacers. These are not considered critical raw materials since they are not subject to supply disruptions or economic dependency, thus making AB-FB a sustainability-friendly alternative and a valid candidate for the future energy storage system.

Overall, this work shows the potential of the Acid/Base Flow Battery in the field of energy storage. Future research could aim at optimising the system in real-world scenarios by coupling the AB-FB with a renewable energy source such as solar or wind power, or by framing it more broadly in polygeneration systems. Further investigation could also focus on optimising the battery for multiple cycles, simulating membranes and/or units from different suppliers. Finally, the economic aspects will have to be thoroughly considered to identify cost-optimal solutions for real-scale applications minimising the levelised cost of storage, which is the essential objective function of practical interest for the assessment of the AB-FB competitiveness.

Nomenclature

Symbols

b (m)	spacer width
C (mol m^{-3})	molar concentration
d (μm)	membrane thickness
d_s (μm)	spacer thickness
D (m^2 s^{-1})	diffusion coefficient
EMF (V)	Nernst potential
f	objective functions vector
F (C mol^{-1})	Faraday constant
g	inequality constraint function
GPD (W m^{-2})	Gross Power Density
h	equality constraint function
i (A m^{-2})	current density
L (m)	spacer length
L_p (ml m^{-2} h^{-1} bar)	osmotic permeability
N (−)	number of triplets
N_{holes} (−)	number of spacer holes
$NED_{v,th}$ (kWh kg^{-1})	theoretical net discharge energy density
NED_v (kWh kg^{-1})	actual net discharge energy density
NPD (W m^{-2})	Net Power Density
$PDUV$ (W L^{-1})	Power density per unit volume
PPD (W m^{-2})	pumping power density
R (Ω cm^2)	generic areal resistance
RTE (−)	Gross Round Trip Efficiency
RTE_{net} (−)	Net Round Trip Efficiency
t (s)	time
u_{ch} (cm s^{-1})	mean channel flow velocity
V (m^3)	generic volume
X_m (mol m^{-3})	fixed charge density in the membrane
x	vector of the decision variables

Greek letters

ε (−)	constraints vector

Subscripts/superscripts

a	acid
b	base
bl	blank
c	charge
d	discharge
in	Inlet or initial
m	membrane phase
s	salt
t	tank
$target$	target concentration

Acronyms/abbreviations

AB-FB	Acid-Base Flow Battery
AEL	Anion-Exchange Layer
AEM	Anion-Exchange Membrane
BMED	Bipolar Membrane ElectroDialysis
BMRED	Bipolar Membrane Reverse ElectroDialysis
BPM	Bipolar Membrane
CAES	Compressed-Air Energy Storage
CEL	Cation-Exchange Layer
CEM	Cation-Exchange Membrane
DLC	Double Layers Capacitor
ED	ElectroDialysis
FES	Flywheel Energy Storage
GA	Genetic Algorithm
GDP	Gross Domestic Product
GPD	Gross Power Density
GVA	Gross Value Added
HFB	Hybrid Flow Battery
MOGA	Multi-Objective Genetic Algorithm
NSGA-II	Non-dominated Sorting Genetic Algorithm II
PHS	Pumped Hydro Storage
PSO	Particle Swarm Optimisation
RED	Reverse ElectroDialysis
RSM	Response Surface Methodology
VRB	Vanadium Redox Flow Battery

CRediT authorship contribution statement

Andrea Culcasi: Methodology, Software, Formal analysis, Investigation, Visualization, Data curation, Validation, Writing - original draft. **Luigi Gurreri:** Conceptualization, Methodology, Validation, Formal analysis, Data curation, Writing – review & editing, Supervision. **Alessandro Tamburini:** Conceptualization, Methodology, Validation, Resources, Writing – review & editing, Supervision, Project administration, Funding acquisition. **Andrea Cipollina:** Conceptualization, Methodology, Validation, Formal analysis, Data curation, Writing – review & editing, Supervision. **I. David L. Bogle:** Conceptualization, Methodology, Validation, Formal analysis, Data curation, Writing – review & editing, Supervision. **Giorgio Micale:** Conceptualization, Methodology, Resources, Writing – review & editing, Supervision, Project administration, Funding acquisition.

Declaration of competing interest

The authors declare that they have no known competing financial interests or personal relationships that could have appeared to influence the work reported in this paper.

Data availability

Data will be made available on request.

Acknowledgments

This work was performed in the framework of the BAoBaB project (*Blue Acid/Base Battery: Storage and recovery of renewable electrical energy by reversible salt water dissociation*). The BAoBaB project has received funding from the European Union's Horizon 2020 Research and Innovation program under Grant Agreement no. 731187 (http://www.baobabproject.eu).

Appendix A. Supplementary data

Supplementary data to this article can be found online at https://doi.org/10.1016/j.est.2023.107429.

References

[1] IEA, Global Energy Review 2021. https://www.iea.org/reports/global-energy-review-2021, 2021 (accessed April 19, 2022).
[2] A. Baldinelli, L. Barelli, G. Bidini, G. Discepoli, Economics of innovative high capacity-to-power energy storage technologies pointing at 100% renewable microgrids, J. Energy Storage 28 (2020), 101198, https://doi.org/10.1016/j.est.2020.101198.
[3] A.M. Elshurafa, The value of storage in electricity generation : a qualitative and quantitative review, J. Energy Storage 32 (2020), 101872, https://doi.org/10.1016/j.est.2020.101872.
[4] Y. Li, X. Zhang, J. Bao, M. Skyllas-Kazacos, Studies on optimal charging conditions for vanadium redox flow batteries, J. Energy Storage 11 (2017) 191–199, https://doi.org/10.1016/j.est.2017.02.008.
[5] Q. Xu, Y.N. Ji, L.Y. Qin, P.K. Leung, F. Qiao, Y.S. Li, H.N. Su, Evaluation of redox flow batteries goes beyond round-trip efficiency: a technical review, J. Energy Storage 16 (2018) 108–115, https://doi.org/10.1016/j.est.2018.01.005.
[6] Z.W. Sun, Z.N. Duan, J.Q. Bai, Y. Wang, Numerical study of the performance of all vanadium redox flow battery by changing the cell structure, J. Energy Storage 29 (2020), 101370, https://doi.org/10.1016/j.est.2020.101370.
[7] M.-Y. Lu, Y.-H. Jiao, X.-Y. Tang, W.-W. Yang, M. Ye, Q. Xu, Blocked serpentine flow field with enhanced species transport and improved flow distribution for vanadium redox flow battery, J. Energy Storage 35 (2021), 102284, https://doi.org/10.1016/j.est.2021.102284.
[8] Z. Huang, A. Mu, L. Wu, H. Wang, Vanadium redox flow batteries: flow field design and flow rate optimization, J. Energy Storage 45 (2022), 103526, https://doi.org/10.1016/j.est.2021.103526.
[9] W.J. van Egmond, M. Saakes, I. Noor, S. Porada, C.J.N. Buisman, H.V.M. Hamelers, Performance of an environmentally benign acid base flow battery at high energy density, Int. J. Energy Res. 42 (2018) 1524–1535, https://doi.org/10.1002/er.3941.
[10] A. Culcasi, L. Gurreri, A. Zaffora, A. Cosenza, A. Tamburini, G. Micale, On the modelling of an Acid/Base flow battery: an innovative electrical energy storage device based on pH and salinity gradients, Appl. Energy 277 (2020), 115576, https://doi.org/10.1016/j.apenergy.2020.115576.
[11] A.H. Galama, J.W. Post, M.A. Cohen Stuart, P.M. Biesheuvel, Validity of the boltzmann equation to describe donnan equilibrium at the membrane–solution interface, J. Membr. Sci. 442 (2013) 131–139, https://doi.org/10.1016/j.memsci.2013.04.022.
[12] R. Pärnamäe, S. Mareev, V. Nikonenko, S. Melnikov, N. Sheldeshov, V. Zabolotskii, H.V.M. Hamelers, M. Tedesco, Bipolar membranes: a review on principles, latest developments, and applications, J. Membr. Sci. 617 (2021), https://doi.org/10.1016/j.memsci.2020.118538.
[13] M. Herrero-Gonzalez, P. Diaz-Guridi, A. Dominguez-Ramos, A. Irabien, R. Ibañez, Highly concentrated HCl and NaOH from brines using electrodialysis with bipolar membranes, Sep. Purif. Technol. 242 (2020), 116785, https://doi.org/10.1016/j.seppur.2020.116785.
[14] A. Zaffora, A. Culcasi, L. Gurreri, A. Cosenza, A. Tamburini, M. Santamaria, G. Micale, Energy harvesting by waste Acid/Base neutralization via bipolar membrane reverse electrodialysis, Energies (Basel) 13 (2020) 5510, https://doi.org/10.3390/en13205510.
[15] F. Sabatino, M. Gazzani, F. Gallucci, M. Van Sint Annaland, Modeling, optimization, and techno-economic analysis of bipolar membrane electrodialysis for direct air capture processes, Ind. Eng. Chem. Res. 61 (2022) 12668–12679, https://doi.org/10.1021/acs.iecr.2c00889.
[16] N. Chindapan, S.S. Sablani, N. Chiewchan, S. Devahastin, Modeling and optimization of electrodialytic desalination of fish sauce using artificial neural networks and genetic algorithm, Food Bioprocess Technol. 6 (2013) 2695–2707, https://doi.org/10.1007/s11947-012-0914-6.
[17] D.W. Bian, S.M. Watson, N.C. Wright, S.R. Shah, T. Buonassisi, D. Ramanujan, I. M. Peters, A.G. Winter, Optimization and design of a low-cost, village-scale, photovoltaic-powered, electrodialysis reversal desalination system for rural India, Desalination 452 (2019) 265–278, https://doi.org/10.1016/j.desal.2018.09.004.
[18] J. Kennedy, R. Eberhart, Particle swarm optimization, in: IEEE International Conference on Neural Networks - Conference Proceedings, 1995, https://doi.org/10.4018/ijmfmp.2015010104.
[19] N.C. Wright, S.R. Shah, S.E. Amrose, A.G. Winter, A robust model of brackish water electrodialysis desalination with experimental comparison at different size scales, Desalination 443 (2018) 27–43, https://doi.org/10.1016/j.desal.2018.04.018.
[20] F. Guesmi, I. Louati, C. Hannachi, B. Hamrouni, Optimization of boron removal from water by electrodialysis using response surface methodology, Water Sci. Technol. 81 (2020) 293–300, https://doi.org/10.2166/wst.2020.105.
[21] F.S. Rohman, N. Aziz, Optimization of batch electrodialysis for hydrochloric acid recovery using orthogonal collocation method, Desalination 275 (2011) 37–49, https://doi.org/10.1016/j.desal.2011.02.025.
[22] F.S. Rohman, N. Aziz, Performance metrics analysis of dynamic multi-objective optimization for energy consumption and productivity improvement in batch electrodialysis, Chem. Eng. Commun. 208 (2021) 517–529, https://doi.org/10.1080/00986445.2019.1674817.
[23] J. Veerman, M. Saakes, S.J. Metz, G.J. Harmsen, Reverse electrodialysis: a validated process model for design and optimization, Chem. Eng. J. 166 (2011) 256–268, https://doi.org/10.1016/j.cej.2010.10.071.
[24] R. Long, B. Li, Z. Liu, W. Liu, Performance analysis of reverse electrodialysis stacks: channel geometry and flow rate optimization, Energy 158 (2018) 427–436, https://doi.org/10.1016/j.energy.2018.06.067.
[25] R. Long, B. Li, Z. Liu, W. Liu, Reverse electrodialysis: modelling and performance analysis based on multi-objective optimization, Energy 151 (2018) 1–10, https://doi.org/10.1016/j.energy.2018.03.003.
[26] M. Ciofalo, M. la Cerva, M. di Liberto, L. Gurreri, A. Cipollina, G. Micale, Optimization of net power density in reverse electrodialysis, Energy 181 (2019) 576–588, https://doi.org/10.1016/j.energy.2019.05.183.
[27] M. La Cerva, M. Di Liberto, L. Gurreri, A. Tamburini, A. Cipollina, G. Micale, M. Ciofalo, Coupling CFD with a one-dimensional model to predict the performance of reverse electrodialysis stacks, J. Membr. Sci. 541 (2017) 595–610, https://doi.org/10.1016/j.memsci.2017.07.030.
[28] P. Faghihi, A. Jalali, An artificial neural network-based optimization of reverse electrodialysis power generating cells using CFD and genetic algorithm, Int. J. Energy Res. (2022) 1–17, https://doi.org/10.1002/er.8379.
[29] A.T. Emrén, V.J.M. Holmström, Energy storage in a fuel cell with bipolar membranes burning acid and hydroxide, Energy 8 (1983) 277–282, https://doi.org/10.1016/0360-5442(83)90103-2.
[30] J. Pretz, E. Staude, Reverse electrodialysis (RED) with bipolar membranes, an energy storage system, berichte Der bunsengesellschaft Für physikalische, Chemie 102 (1998) 676–685, https://doi.org/10.1002/bbpc.19981020412.
[31] E.K. Zholkovskij, M.C. Müller, E. Staude, The storage battery with bipolar membranes, J. Membr. Sci. 141 (1998) 231–243, https://doi.org/10.1016/S0376-7388(97)00306-2.
[32] J.H. Kim, J.H. Lee, S. Maurya, S.H. Shin, J.Y. Lee, I.S. Chang, S.H. Moon, Proof-of-concept experiments of an acid-base junction flow battery by reverse bipolar electrodialysis for an energy conversion system, Electrochem. Commun. 72 (2016) 157–161, https://doi.org/10.1016/j.elecom.2016.09.025.
[33] J. Xia, G. Eigenberger, H. Strathmann, U. Nieken, Flow battery based on reverse electrodialysis with bipolar membranes: single cell experiments, J. Membr. Sci. 565 (2018) 157–168, https://doi.org/10.1016/j.memsci.2018.07.073.
[34] J. Xia, G. Eigenberger, H. Strathmann, U. Nieken, Acid-base flow battery, based on reverse electrodialysis with Bi-polar membranes: stack experiments, Processes 8 (2020) 99, https://doi.org/10.3390/pr8010099.
[35] R. Pärnamäe, L. Gurreri, J. Post, W.J. van Egmond, A. Culcasi, M. Saakes, J. Cen, E. Goosen, A. Tamburini, D.A. Vermaas, M. Tedesco, The Acid-Base flow battery: sustainable energy storage via reversible water dissociation with bipolar membranes, Membranes (Basel) 10 (2020) 409, https://doi.org/10.3390/membranes10120409.
[36] A. Culcasi, L. Gurreri, G. Micale, A. Tamburini, Bipolar membrane reverse electrodialysis for the sustainable recovery of energy from pH gradients of industrial wastewater: performance prediction by a validated process model, J. Environ. Manag. 287 (2021), 112319, https://doi.org/10.1016/j.jenvman.2021.112319.
[37] A. Culcasi, L. Gurreri, A. Cipollina, A. Tamburini, G. Micale, A Comprehensive Multi-scale Model for Bipolar Membrane Electrodialysis (BMED) 437, 2022, https://doi.org/10.1016/j.cej.2022.135317.
[38] Y. Cui, Z. Geng, Q. Zhu, Y. Han, Review: multi-objective optimization methods and application in energy saving, Energy 125 (2017) 681–704, https://doi.org/10.1016/j.energy.2017.02.174.
[39] Y.V. Haimes, L.S. Lasdon, D.A. Wismer, On a bicriterion formulation of the problems of integrated system identification and system optimization, IEEE Trans Syst Man Cybern. (1971) 296–297, https://doi.org/10.1109/TSMC.1971.4308298. SMC-1.
[40] G.P. Rangaiah, A. Bonilla-Petriciolet, Multi-objective Optimization in Chemical Engineering, John Wiley & Sons Ltd, Oxford, UK, 2013, https://doi.org/10.1002/9781118341704.
[41] A. Castillo, D.F. Gayme, Grid-scale energy storage applications in renewable energy integration: a survey, Energy Convers. Manag. 87 (2014) 885–894, https://doi.org/10.1016/j.enconman.2014.07.063.
[42] G.J. May, A. Davidson, B. Monahov, Lead batteries for utility energy storage: a review, J. Energy Storage 15 (2018) 145–157, https://doi.org/10.1016/j.est.2017.11.008.
[43] E. Bullich-Massagué, F.-J. Cifuentes-García, I. Glenny-Crende, M. Cheah-Mañé, M. Aragüés-Peñalba, F. Díaz-González, O. Gomis-Bellmunt, A review of energy storage technologies for large scale photovoltaic power plants, Appl. Energy 274 (2020), 115213, https://doi.org/10.1016/j.apenergy.2020.115213.

[44] S. Koohi-Fayegh, M.A. Rosen, A review of energy storage types, applications and recent developments, J. Energy Storage 27 (2020), 101047, https://doi.org/10.1016/j.est.2019.101047.
[45] D.O. Akinyele, R.K. Rayudu, Review of energy storage technologies for sustainable power networks, Sustain. Energy Technol. Assess. 8 (2014) 74–91, https://doi.org/10.1016/j.seta.2014.07.004.
[46] A. Castillo, D.F. Gayme, Grid-scale energy storage applications in renewable energy integration: a survey, Energy Convers. Manag. 87 (2014) 885–894, https://doi.org/10.1016/j.enconman.2014.07.063.
[47] G.A. Blengini, C. el Latunussa, U. Eynard, Study on the Eu's List of Critical Raw Materials - Critical Raw Materials Factsheets, 2020, https://doi.org/10.2873/11619.
[48] E. Lewicka, K. Guzik, K. Galos, On the possibilities of critical raw materials production from the Eu's primary sources, Resources 10 (2021), https://doi.org/10.3390/RESOURCES10050050.
[49] P. Viebahn, O. Soukup, S. Samadi, J. Teubler, K. Wiesen, M. Ritthoff, Assessing the need for critical minerals to shift the german energy system towards a high proportion of renewables, Renew. Sust. Energ. Rev. 49 (2015) 655–671, https://doi.org/10.1016/j.rser.2015.04.070.
[50] E. Blumbergs, V. Serga, E. Platacis, M. Maiorov, A. Shishkin, Cadmium recovery from spent Ni-Cd batteries: a brief review, Metals (Basel) 11 (2021) 1–14, https://doi.org/10.3390/met11111714.
[51] N. Chawla, M. Safa, Sodium batteries: a review on sodium-sulfur and sodium-air batteries, Electronics (Switzerland) 8 (2019), https://doi.org/10.3390/electronics8101201.
[52] A. Van Zyl, Review of the zebra battery system development, Solid State Ionics 86–88 (1996) 883–889.
[53] L. Gao, Z. Li, Y. Zou, S. Yin, P. Peng, Y. Shao, X. Liang, A high-performance aqueous zinc-bromine static battery, IScience 23 (2020), 101348, https://doi.org/10.1016/j.isci.2020.101348.
[54] M.M. Rahman, E. Gemechu, A.O. Oni, A. Kumar, Energy and environmental footprints of flywheels for utility-scale energy storage applications, E-Prime 1 (2021), 100020, https://doi.org/10.1016/j.prime.2021.100020.
[55] D. Schrijvers, A. Hool, G.A. Blengini, W.Q. Chen, J. Dewulf, R. Eggert, L. van Ellen, R. Gauss, J. Goddin, K. Habib, C. Hagelüken, A. Hirohata, M. Hofmann-Amtenbrink, J. Kosmol, M. Le Gleuher, M. Grohol, A. Ku, M.H. Lee, G. Liu, K. Nansai, P. Nuss, D. Peck, A. Reller, G. Sonnemann, L. Tercero, A. Thorenz, P. A. Wäger, A review of methods and data to determine raw material criticality, Resour. Conserv. Recycl. 155 (2020), 104617, https://doi.org/10.1016/j.resconrec.2019.104617.
[56] K. Scott, RECYCLING | Nickel–metal hydride batteries, in: Encyclopedia of Electrochemical Power Sources, Elsevier B.V., 2009, pp. 199–208, https://doi.org/10.1016/B978-044452745-5.00401-9.
[57] S.C. Johnson, F.Todd Davidson, J.D. Rhodes, J.L. Coleman, S.M. Bragg-Sitton, E. J. Dufek, M.E. Webber, Selecting Favorable Energy Storage Technologies for Nuclear Power, Elsevier Inc., 2018, https://doi.org/10.1016/B978-0-12-813975-2.00005-3.
[58] A. Ciotola, M. Fuss, S. Colombo, W. Poganietz, The potential supply risk of vanadium for the renewable energy transition in Germany, J. Energy Storage 33 (2021), 102094, https://doi.org/10.1016/j.est.2020.102094.
[59] A.R. Mainar, E. Iruin, L.C. Colmenares, A. Kvasha, I. De Meatza, M. Bengoechea, O. Leonet, I. Boyano, Z. Zhang, J.A. Blazquez, An overview of progress in electrolytes for secondary zinc-air batteries and other storage systems based on zinc, J. Energy Storage 15 (2018) 304–328, https://doi.org/10.1016/j.est.2017.12.004.
[60] M.C. Díaz-Ramírez, M. Blecua-de-Pedro, A.J. Arnal, J. Post, Acid/base flow battery environmental and economic performance based on its potential service to renewables support, J. Clean. Prod. 330 (2022), https://doi.org/10.1016/j.jclepro.2021.129529.